Coherent Fano resonances in a plasmonic nanocluster enhance optical four-wave mixing

Yu Zhang[a,b], Fangfang Wen[b,c], Yu-Rong Zhen[a,b], Peter Nordlander[a,b,d], and Naomi J. Halas[a,b,c,d,1]

Departments of [a]Physics and Astronomy, [c]Chemistry, and [d]Electrical and Computer Engineering, and [b]Laboratory for Nanophotonics, Rice University, Houston, TX 77005

Edited by David A. B. Miller, Stanford University, Stanford, CA, and approved April 23, 2013 (received for review November 22, 2012)

Plasmonic nanoclusters, an ordered assembly of coupled metallic nanoparticles, support unique spectral features known as Fano resonances due to the coupling between their subradiant and superradiant plasmon modes. Within the Fano resonance, absorption is significantly enhanced, giving rise to highly localized, intense near fields with the potential to enhance nonlinear optical processes. Here, we report a structure supporting the coherent oscillation of two distinct Fano resonances within an individual plasmonic nanocluster. We show how this coherence enhances the optical four-wave mixing process in comparison with other double-resonant plasmonic clusters that lack this property. A model that explains the observed four-wave mixing features is proposed, which is generally applicable to any third-order process in plasmonic nanostructures. With a larger effective susceptibility $\chi^{(3)}$ relative to existing nonlinear optical materials, this coherent double-resonant nanocluster offers a strategy for designing high-performance third-order nonlinear optical media.

nanostructured materials | nonlinear optics | phase matching

Traditionally, nonlinear optical phenomena have relied on crystalline media that combine material susceptibilities and phase matching to optimize nonlinear optical processes. It has recently been shown that certain plasmonic nanostructures can produce an enhanced nonlinear response when excited at their resonant frequency (1, 2). Phase-matching requirements (3–5) for nonlinear optics in macroscopic media are usually optimally fulfilled at nanoscale dimensions [$\mathrm{sinc}^2(\Delta k\, z/2) \sim 1$ for small z, where z is the propagation distance through the medium]. For plasmonic nanostructures, the most important property for the enhancement of nonlinear properties is their increased local fields at resonance, which can provide larger effective susceptibilities than their intrinsic material susceptibility.

In the third-order nonlinear process of four-wave mixing (FWM), two external fields $E_0(\omega_1)$ and $E_0(\omega_2)$ are simultaneously incident on the nanostructure, inducing local fields $E(\omega_1)$ and $E(\omega_2)$; absorbing two ω_2 and one ω_1 photons and emitting a photon at $\omega_{\mathrm{FWM}} = 2\omega_2 - \omega_1$ (Fig. 1*A*) (3). The electromagnetic FWM enhancement $G_{\mathrm{FWM}} = |E(\omega_2)/E_0(\omega_2)|^4 \cdot |E(\omega_1)/E_0(\omega_1)|^2$ thus depends on the field enhancements at the input frequencies. Fano-resonant structures can exhibit very large local field enhancements (6, 7), making these structures prime candidates for nonlinear frequency generation. Although previous studies of nonlinear plasmonics used nanostructures with a single dipolar resonance (8, 9), in a multiinput process such as FWM, the conversion efficiency is expected to be further enhanced if the plasmon modes of the nanostructure are resonant with both input frequencies (10).

In this study, we demonstrate highly efficient FWM from a plasmonic nanocluster that supports two distinct Fano resonances (FRs) (6, 7, 11–14). When excited by a coherent source, the two spatially coherent FRs oscillate collectively, in a mixed frequency analog to a two-state quantum system, where the electric fields from the two modes add coherently, resulting in strong field enhancements. In comparison, plasmonic nanostructures with resonances at the same two frequencies that lack coherence are found to give rise to lower FWM efficiencies, while providing similar linear optical properties.

The geometry of the nanocluster was designed such that its FRs was tuned to the two excitation frequencies needed for FWM. The nanocluster, composed of a central disk, an inner ring of disks, and a degenerate outer ring of disks (Fig. 1*B*, *Inset*), belongs to the D_{6h} symmetry group (12). Measured and calculated linear scattering spectra (Fig. 1*B*) reveal two prominent scattering minima. The origin of these spectral dips can be understood by examining the charge densities $\rho(\mathbf{r}, t)$ at the spectral minima (Fig. 1*C*), where the structure supports oscillations of the central disk and the inner and outer rings of disks. At the minimum at 800-nm wavelength, the center particle dipole oscillates out-of-phase with both the inner and outer collective ring oscillations. However, at the minimum at 670-nm wavelength, the center particle dipole oscillates out-of-phase with the inner ring but in-phase with the outer ring.

When both FRs of the nanocluster are excited simultaneously (by two coherent beams), the plasmons oscillate in a mixed frequency "coherent state." In this mode, the charge oscillation of the central disk switches rapidly between an in-phase and out-of-phase motion with respect to the outer ring, in each case corresponding to the oscillatory behavior of one of the FRs (Fig. 1*D*; see details in Fig. S1 and *SI Text*). By performing a discrete Fourier transform (15) on the time series of charge densities $\rho(\mathbf{r}, t)$ at each position $\mathbf{r}$, this coherent state, with a period T_{coherent} of ∼13.35 fs, can be decomposed into two discrete FR eigenmodes with $\rho(\mathbf{r}, \omega)$ at 800 (T_1 of ∼2.67 fs) and 670 nm (T_2 of ∼2.23 fs) (Movies S1, S2, and S3). The coherent mode has a period equal to the time when the two discrete FRs have the same phase ($T_{\mathrm{coherent}} \sim 5T_1 \sim 6T_2$), undergoing ∼15 periods during the pulse duration used in the experiment (τ of ∼200 fs). For the coherent state, enhanced local fields at multiple resonant frequencies overlap not only in time but also in space, contributing to the nonlinear optical wave mixing.

FWM measurements on individual nanoclusters were performed using a specially designed optical microscope with a high-precision positioning stage that facilitates focusing (details in Fig. S2 and *SI Text*). Two linearly (*x*-) polarized, collinear, and coherent pulse trains (along the *z* direction) at $\lambda_1 = 800$ nm and $\lambda_2 = 670$ nm, resonant with both FRs were focused onto an individual nanocluster (in the *x*–*y* plane), resulting in a spot size of ∼1 μm. Both beams behave like normal-incidence plane waves on the nanocluster, and the phase-matching factor was calculated to be 0.99 in this case (see a detailed analysis in Fig. S3 and *SI Text*). The scattered radiation was collected by another focusing objective

Author contributions: P.N. and N.J.H. designed research; Y.Z. performed research; F.W. and Y.-R.Z. contributed new reagents/analytic tools; Y.Z. and Y.-R.Z. analyzed data; and Y.Z., P.N., and N.J.H. wrote the paper.

The authors declare no conflict of interest.

Freely available online through the PNAS open access option.

This article is a PNAS Direct Submission.

[1]To whom correspondence should be addressed. E-mail: halas@rice.edu.

This article contains supporting information online at www.pnas.org/lookup/suppl/doi:10.1073/pnas.1220304110/-/DCSupplemental.

Fig. 1. FWM configuration and characterization of the double Fano resonant plasmonic nanocluster. (*A*) FWM configuration in a single nanocluster, where two coherent inputs at frequencies ω_1 and ω_2 generate a plasmon-enhanced FWM signal $\omega_{FWM} = 2\omega_2 - \omega_1$. (*B*) Experimental (black) and calculated (green) dark-field scattering spectra of the nanocluster obtained with horizontal (*x*-) polarization. Two prominent minima at 800 and 670 nm are labeled by brown and orange dashed lines. *Inset* shows an SEM image of the nanocluster. (Scale bar, 100 nm.) All disk diameters are 120 nm with 50-nm heights and ~18-nm gaps. The superimposed yellow dashed lines denote the central disk, inner and outer disk rings of the nanocluster. The red arrow indicates the incident polarization. (*C* and *D*) Snapshots of simulated charge densities $\rho(\mathbf{r}, t)$ on the top surface of the nanocluster for the 800- and 670-nm FRs at $t = 0$ (*C*), and for the coherent state at three different times (*D*). The black arrows correspond to local E-field directions.

in transmission and analyzed with a CCD-coupled spectrometer. Only the case in which both lasers were *x*-polarized was investigated, because this configuration generated the strongest FWM signal. The total average applied power ranged from 1 to 3 μW (peak intensities of 0.13~0.4 GW cm^{-2}), and measurements were performed on six different nanoclusters to ensure statistical validity. All nanoclusters underwent a pulsed laser annealing procedure using 3.8 μW total power for 4 min to stabilize the nanostructure before data collection (Fig. S4).

A characteristic FWM output spectrum consists of a sharply peaked signal centered at $\lambda_{FWM} = 576$ nm with $\Delta\lambda_{FWM} = 5.3$ nm, on top of a significantly weaker, broadband multiphoton luminescence signal (16) (Fig. 2*A*, green). The Gaussian line shape FWHM of the incident beams was measured to be $\Delta\lambda_1 = 5.3$ nm and $\Delta\lambda_2 = 5.5$ nm (Fig. 2*A*, red). If one considers the timescale of FWM generation as being $\sim\tau$, the estimated FWM bandwidth should be proportional to $1/\tau$, which is close to the observed result. Additionally, we observed another FWM signal centered at $\lambda_{FWM2} = 993$ nm with $\Delta\lambda_{FWM2}$ of ~4 nm (Fig. S5), due to the complementary $\omega_{FWM2} = 2\omega_1 - \omega_2$ process. Because this signal lies at the limit of our CCD detection range, we focused on the 576-nm FWM signal only.

The FWM signal was observed to follow a cubic power law behavior as a function of total input power ($P_{tot} = 1.05$~2.9 μW, using P_1:P_2 = 1:2) (Fig. 2*B*). This response scales quadratically with the P_2 input power ($P_2 = 0.84$~1.9 μW, using $P_1 = 1.1$ μW), and linearly with P_1 input power ($P_1 = 0.4$~1 μW, using $P_2 = 1.9$ μW). All data points in this regime follow a simple power law, indicating that we are not in a regime of plasmon saturation (17). Increasing the input power further causes optical damage of the sample: when this occurs, the FWM signal gradually and irreversibly decreases. We calculated the nonlinear cross-section for

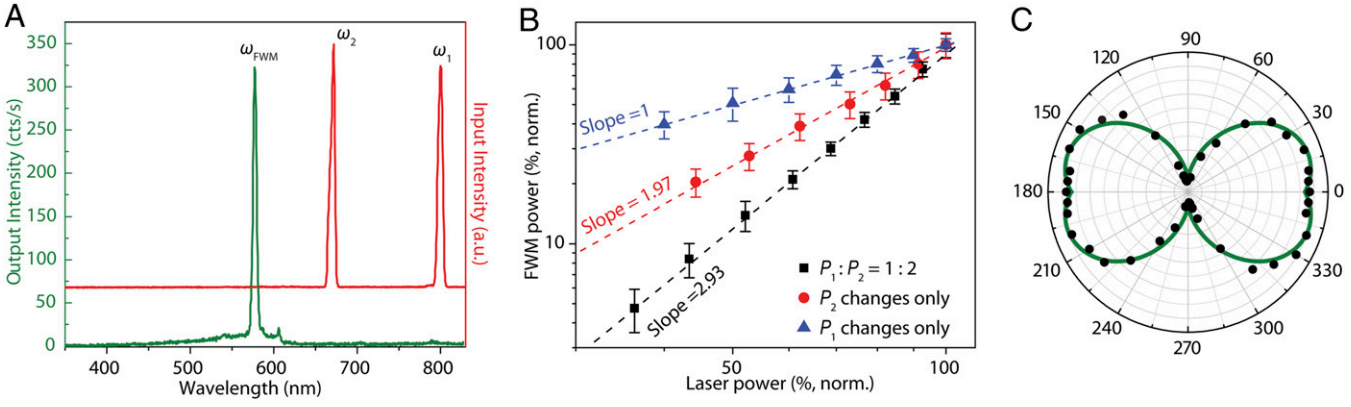

Fig. 2. FWM experiments by individual nanoclusters. (*A*) Spectra of the two input laser beams (red), and a FWM output signal generated by $P_1 = 1$ μW and $P_2 = 1.9$ μW (green). The small spectral feature at ~615 nm is the edge of the short-pass filter used to block the excitation beams. (*B*) Normalized FWM power versus normalized total input power P_{tot} (black squares), P_2 only (red circles), and P_1 only (blue triangles) on a log-log scale. The dashed lines are linear fits of the experimental data. Error bars represent the SDs of signals from six individual nanoclusters, arising mainly from fabrication irregularities. (*C*) Polar plots show the measured (black circles) and calculated (green curve) FWM polarization by two *x*-polarized lasers. The latter is calculated based on Fig. 3*C*.

the nanocluster to be $\sigma^{(3)} = 1.41\times 10^{-12}$ cm^2, and its effective susceptibility $\chi^{(3)}$ is 4.65×10^{-15} m^2 V^{-2} (3.35×10^{-7} esu), taking into account the instrument efficiency (3). This value is much larger than that of nonresonant dielectrics (3) (10^{-22}~10^{-18} m^2 V^{-2}), semiconductors (18) (~10^{-12} esu) or nonlinear crystals (19) (10^{-14}~10^{-13} esu), and among the highest reported for metallic nanoparticles (20–23) (10^{-12}~10^{-7} esu), which we attribute to the enhancement provided by the coherently coupled FRs in the nanostructure. The polarization dependence of the FWM signal has an unusual butterfly-like profile, with its maximum intensities near 20° and 160° (Fig. 2*C*, black circles). The FWM light has a nonzero *y*-component, despite the fact that both pump lasers are purely *x*-polarized (Fig. S6). These results are distinct from previous studies (9, 24) in which the FWM was linearly polarized for either parallel or oblique incidence.

We have developed a simple model to explain the origin and characteristics of FWM on a plasmonic nanocluster. In degenerate FWM, the two local fields $\tilde{\mathbf{E}}(\mathbf{r},\omega_1,t)$ and $\tilde{\mathbf{E}}(\mathbf{r},\omega_2,t)$ induce a nonlinear polarization as follows:

$$\mathbf{P}^{(3)}(\mathbf{r},\omega_{\mathrm{FWM}}) = \varepsilon_0 \overleftrightarrow{\chi}^{(3)}(-\omega_{\mathrm{FWM}};\ \omega_2,\omega_2,\ -\omega_1)\vdots \mathbf{E}(\mathbf{r},\omega_2)\mathbf{E}(\mathbf{r},\omega_2)\mathbf{E}^*(\mathbf{r},\omega_1), \quad [1]$$

where $\mathbf{E}(\mathbf{r},\omega) = \tilde{\mathbf{E}}(\mathbf{r},\omega,t)/e^{-iwt}$ is the amplitude of the time-harmonic fields; the susceptibility tensor $\overleftrightarrow{\chi}^{(3)}$ accounts for the intrinsic third-order nonlinear response of the material(s) and in turn gives rise to a FWM field $\mathbf{E}(\mathbf{r},\omega_{\mathrm{FWM}}) = \mathbf{P}^{(3)}(\mathbf{r},\omega_{\mathrm{FWM}})/\varepsilon_0 n^2(\omega_{\mathrm{FWM}})$ radiating at $\omega_{\mathrm{FWM}} = 2\omega_2 - \omega_1$. When both incoming frequencies are incident on the nanocluster and resonant with its FRs, their enhanced local fields overlap spatially in the nanocluster gap regions (Fig. 3*A*). These intense fields give rise to the large effective $\chi^{(3)}$ (8, 17). At optical frequencies, plasmon-enhanced local fields are confined within a thin layer on each metal surface, in the direction of the surface normal (2) with a dominant surface nonlinearity (25, 26); thus, Eq. **1** can be transformed into the surface coordinate system where only the normal component is considered as follows:

$$E_{\mathrm{s,n}}(\omega_{\mathrm{FWM}}) = \chi^{(3)}_{\mathrm{s,nnnn}} E^2_{\mathrm{s,n}}(\omega_2) E_{\mathrm{s,n}}(\omega_1)/n^2(\omega_{\mathrm{FWM}}), \quad [2]$$

where $\chi_{\mathrm{s,nnnn}}{}^{(3)}$ is assumed to be a constant over the metal surfaces for simplicity.

Because the generated FWM field oscillates rapidly with time, the measured signal is the time-integrated intensity $I(\omega_{\mathrm{FWM}}) \propto E^2(\omega_{\mathrm{FWM}})$. A generalized formula is obtained for FWM fields enhanced by plasmonic nanostructures (Fig. 3*B*):

$$\left\langle \tilde{E}_{\mathrm{s,n}}(\omega_{\mathrm{FWM}},t)\right\rangle = \left[\frac{1}{T}\int_0^T E^2_{\mathrm{s,n}}(\omega_{\mathrm{FWM}})\cos^2(\omega_{\mathrm{FWM}}t)dt\right]^{\frac{1}{2}} = \frac{\sqrt{2}}{2}\chi^{(3)}_{\mathrm{s,nnnn}} E^2_{\mathrm{s,n}}(\omega_2) E_{\mathrm{s,n}}(\omega_1)/n^2(\omega_{\mathrm{FWM}}). \quad [3]$$

The polarization of each FWM photon is perpendicular to the Au side walls in the *x*–*y* plane, provided that the photon polarization is the same as its local fields. The FWM field map can be decomposed into *x* and *y* components (Fig. 3*C*), and then the far-field FWM polarization is obtained by integrating over the Au surfaces as follows:

$$I_{\mathrm{FWM}}(\theta) \propto \int \left[\left\langle \tilde{E}_{\mathrm{x}}(\omega_{\mathrm{FWM}},t)\right\rangle \left|\cos\theta\right| + \left\langle \tilde{E}_{\mathrm{y}}(\omega_{\mathrm{FWM}},t)\right\rangle \left|\sin\theta\right|\right]^2 ds, \quad [4]$$

where θ is the angle between the output polarizer and the *x* axis. The calculated FWM polarization polar plot (Fig. 2*C*, green curve) has a small *y* component at $\theta = 90°$ and a much larger *x* component that is slightly reduced at $\theta = 0°$. The degree of polarization, $P_{\mathrm{d}} = (|I_{\mathrm{x}} - I_{\mathrm{y}}|)/(|I_{\mathrm{x}} + I_{\mathrm{y}}|) = 0.64$, is consistent with experimental measurements. This unusual polarization behavior results because some FWM hotspots are not parallel to either the *x* or *y* axis (e.g., i, ii, and iii in Fig. 3*B*) and therefore contribute partially to each of the orthogonal components of the emitted light.

To further investigate the specific effect of coherent FRs on the enhancement of optical FWM, two nanocluster "controls" were designed: (*i*) one with two coherent bright modes, where charges

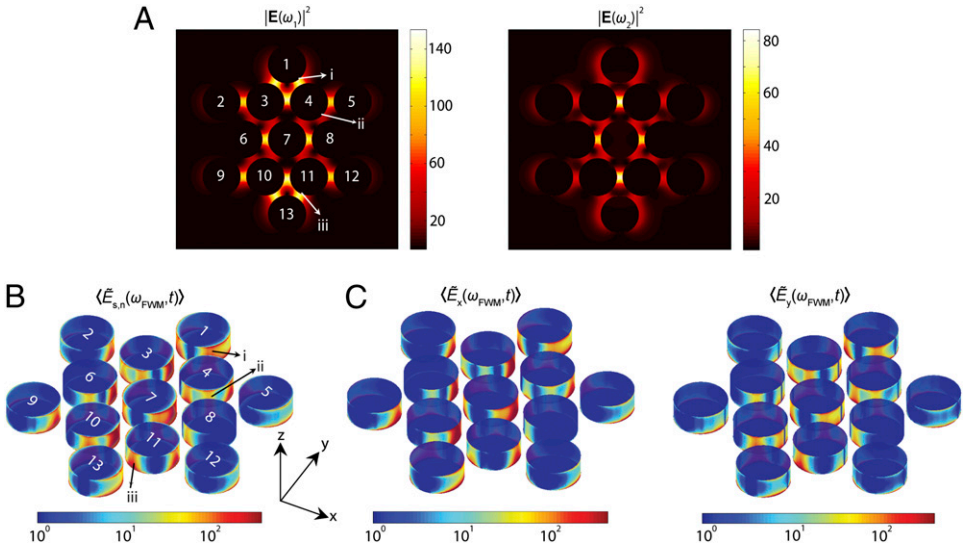

Fig. 3. FDTD calculated near-field maps of the nanocluster. (*A*) The field enhancement intensity (E^2) evaluated at midheight of the nanocluster at λ_1 = 800 nm (*Left*) and λ_2 = 670 nm (*Right*). (*B*) Time-averaged FWM fields generated on the Au nanocluster surfaces. The color scales assume unity incident fields and $\chi_s{}^{(3)}n^{-2}$. In *A* and *B*, the overlaid disk indices are guides to the eye; i, ii, and iii point to three hotspots. (*C*) Time-averaged *x* (*Left*) and *y* (*Right*) components of the FWM fields on the nanocluster surfaces.

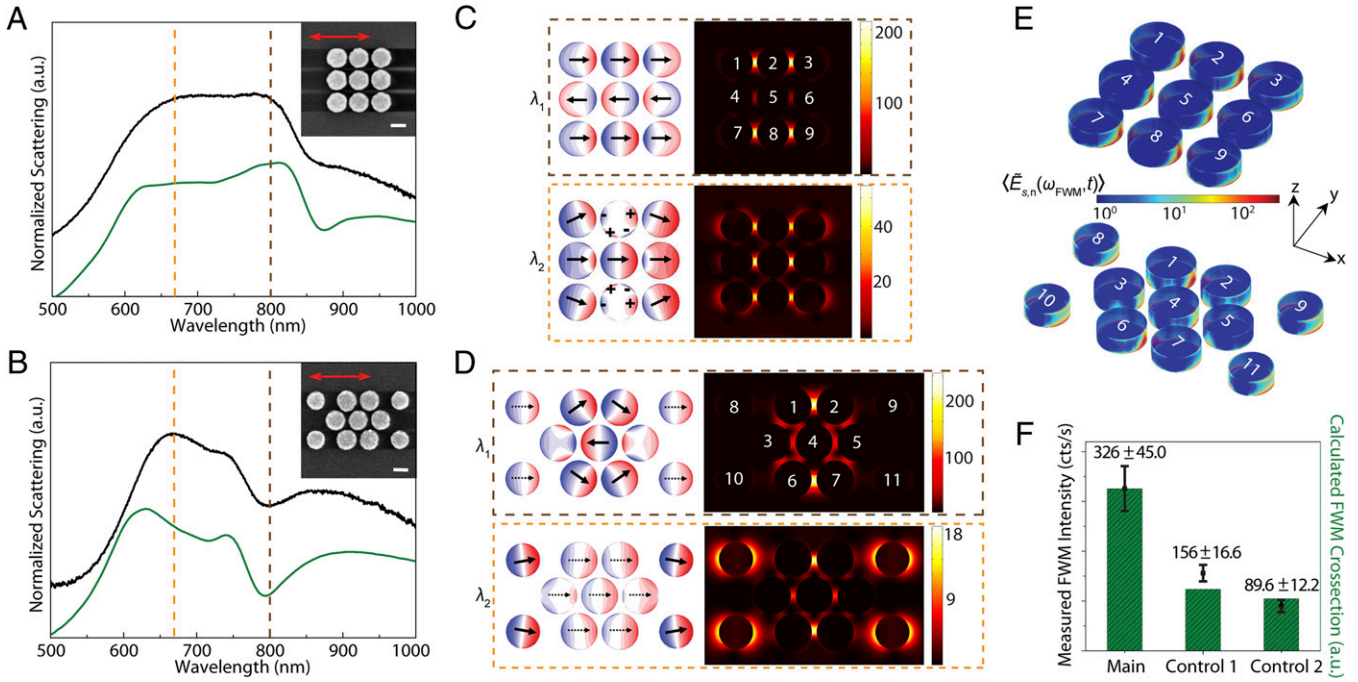

Fig. 4. FWM control experiments. (*A* and *B*) Experimental (black) and calculated (green) dark-field scattering spectra of two nanoclusters for control experiments, obtained with horizontal (*x*) polarization. Both structures have double resonances, indicated by the brown (800 nm) and orange (670 nm) dashed lines. *Insets* are SEM images of these nanoclusters. (Scale bars, 100 nm.) The red arrows indicate the incident polarization. In *A*, all disk diameters are 144 nm with ~18-nm gaps. In *B*, the nanocluster is formed by a heptamer surrounded by four corner disks. Heptamer disks are 135 nm in diameters with ~18-nm gap; corner disks are 124 nm with ~80-nm spacing from heptamer disks along *x* direction. (*C* and *D*) Simulated charge distributions (*Left*) and field enhancement intensities E^2 (*Right*) for two control cases at $\lambda_1 = 800$ nm (brown dashed box) and $\lambda_2 = 670$ nm (orange dashed box). The black arrows indicate local E-field directions. (*E*) Time-averaged FWM fields on nanocluster surfaces. The color scales assume unity incident fields and $\chi_s^{(3)} n^{-2}$. In *C*, *D*, and *E*, the overlaid disk indexes are guides to the eye. (*F*) Measured FWM intensities (error bars) and calculated FWM cross-section (green bars) for all three structures.

oscillate in dipole–dipole (antibonding) and dipole–quadrupole modes (Fig. 4 *A* and *C*); and (*ii*) one with two spatially incoherent (decoupled) oscillations of a subradiant heptamer dark mode and a dipole bright mode supported by the corner disks (Fig. 4 *B* and *D*). In all cases, the plasmon resonant features were designed to correspond to the two FWM input frequencies. Besides the double-resonant conditions fulfilled by these structures, there are other factors affecting the FWM efficiency, which we attempt to maintain as consistently as possible for all three cluster geometries. Because larger particles usually give rise to stronger signals, all structures were designed with same volume of Au for comparison. The sizes of the gaps also strongly affect the nonlinear responses of the clusters, where stronger signals come from smaller gaps (8, 10, 27); thus, they were made identical in all three geometries, except for the ~80-nm decoupling spacing in case *ii* (Fig. 4 *A* and *B*, *Insets*). Fig. 4*E* shows the time-averaged FWM fields. By integrating the square modulus of the FWM field over the disk surfaces shown in Fig. 3*B* or 4*E*, relative FWM cross sections (∝ conversion efficiencies) can be calculated for these three structures, which agree well with the measured FWM intensities by $P_1 = 1$ μW and $P_2 = 1.9$ μW (Fig. 4*F*). Comparison between all three cluster geometries shows that, although all cluster geometries show a significant FWM enhancement, the structure supporting two coherent FRs provides the highest FWM enhancement among these three types of double-resonant structures by nominally a factor of 2~4. We attribute this as being due to the reduced light scattering and intense local fields of the coherently coupled (spatially overlapping) FRs relative to the other cluster geometries. Control (*ii*), where the two resonances are spatially decoupled, has the lowest FWM enhancement.

In conclusion, we report a plasmonic nanocluster that supports two FRs in a coherent state, a temporally oscillating superposition of two spatially coherent subradiant modes. Time-resolved field investigations reveal the ultrafast dynamics of this coherent state, suggesting that dynamical studies may lead to a greater understanding of coherence in plasmonic nanocomplexes. We have also shown that this nanostructure provides an outstanding resonant enhancement of optical FWM, providing significantly greater enhancement of this process than similarly sized nanoclusters with double resonances of different types. The extremely large effective $\chi^{(3)}$ for this nanocluster strongly suggests its use in high-performance synthetic nonlinear optical materials, which would provide new strategies for optical information processing, sensors, and detectors, and new types of optoelectronic devices.

Materials and Methods

Sample Preparation and Characterization. These structures were fabricated by standard positive-resist electron beam lithography for patterning a 50-nm–thick Au on a 1-nm Ti adhesive layer, which had first been evaporated onto an ultra-smooth fused silica substrate (surface finish 10/5, SVM). The fabricated nanoclusters were arranged in a 5 × 5 array with 10-μm intercluster distances to avoid coupling effects during single-particle measurements. Dark-field scattering spectra were collected by a custom-built microscope with ~35° incidence (microscope: Axiovert 200 MAT, Zeiss; objective: 50×/0.55 NA Epiplan-Neofluar, Zeiss; spectrograph: SP2150, PI/Acton; CCD: PIXIS 400BR, PI/Acton).

Simulation Method. Numerical studies of the electromagnetic responses were performed using the finite-difference time-domain (FDTD) commercial software (Lumerical FDTD Solutions 7.5.3) with normal incidence. The top-view geometries were chosen to closely match SEM images, and the heights used were the Au thickness deposited during sample fabrication. The empirical bulk dielectric function (28) was used for Au and $\varepsilon = 2.10$ for the infinite fused silica substrate. Charge density was obtained by calculating the difference of the normal component of the electric field above and below the Au surface (Gauss's law).

ACKNOWLEDGMENTS. We thank Nche Tumasang Fofang, Na Liu, Jared Day, Alexander Urban, J. Britt Lassiter, and Shaunak Mukherjee for assistance. This work was supported by Department of Defense National Security Science and Engineering Faculty Fellowship N00244-09-1-0067, Air Force Office of Scientific Research Grant F49620-03-C-0068, Office of Naval Research Grant N00014-10-1-0989, and The Robert A. Welch Foundation Grants C-1220 and C-1222.

1. Klein MW, Enkrich C, Wegener M, Linden S (2006) Second-harmonic generation from magnetic metamaterials. *Science* 313(5786):502–504.
2. Zhang Y, Grady NK, Ayala-Orozco C, Halas NJ (2011) Three-dimensional nanostructures as highly efficient generators of second harmonic light. *Nano Lett* 11(12): 5519–5523.
3. Boyd RW (2008) *Nonlinear Optics* (Academic, Boston), 3rd Ed.
4. Ellenbogen T, Voloch-Bloch N, Ganany-Padowicz A, Arie A (2009) Nonlinear generation and manipulation of Airy beams. *Nat Photonics* 3(7):395–398.
5. Corcoran B, et al. (2009) Green light emission in silicon through slow-light enhanced third-harmonic generation in photonic-crystal waveguides. *Nat Photonics* 3(4):206–210.
6. Luk'yanchuk B, et al. (2010) The Fano resonance in plasmonic nanostructures and metamaterials. *Nat Mater* 9(9):707–715.
7. Ye J, et al. (2012) Plasmonic nanoclusters: Near field properties of the Fano resonance interrogated with SERS. *Nano Lett* 12(3):1660–1667.
8. Grady NK, Knight MW, Bardhan R, Halas NJ (2010) Optically-driven collapse of a plasmonic nanogap self-monitored by optical frequency mixing. *Nano Lett* 10(4): 1522–1528.
9. Genevet P, et al. (2010) Large enhancement of nonlinear optical phenomena by plasmonic nanocavity gratings. *Nano Lett* 10(12):4880–4883.
10. Harutyunyan H, Volpe G, Quidant R, Novotny L (2012) Enhancing the nonlinear optical response using multifrequency gold-nanowire antennas. *Phys Rev Lett* 108(21): 217403.
11. Fan JA, et al. (2010) Self-assembled plasmonic nanoparticle clusters. *Science* 328(5982): 1135–1138.
12. Dregely D, Hentschel M, Giessen H (2011) Excitation and tuning of higher-order Fano resonances in plasmonic oligomer clusters. *ACS Nano* 5(10):8202–8211.
13. Hentschel M, et al. (2010) Transition from isolated to collective modes in plasmonic oligomers. *Nano Lett* 10(7):2721–2726.
14. Liu H, et al. (2011) Linear and nonlinear Fano resonance on two-dimensional magnetic metamaterials. *Phys Rev B* 84(23):235437.
15. Oppenheim AV, Schafer RW, Buck JR (1998) *Discrete-Time Signal Processing* (Prentice-Hall, Upper Saddle River), 2nd Ed.
16. Farrer RA, Butterfield FL, Chen VW, Fourkas JT (2005) Highly efficient multiphoton-absorption-induced luminescence from gold nanoparticles. *Nano Lett* 5(6):1139–1142.
17. Pelton M, Liu M, Park S, Scherer NF, Guyot-Sionnest P (2006) Ultrafast resonant optical scattering from single gold nanorods: Large nonlinearities and plasmon saturation. *Phys Rev B* 73(15):155419.
18. Gu T, et al. (2012) Regenerative oscillation and four-wave mixing in graphene optoelectronics. *Nat Photonics* 6(8):554–559.
19. Ganeev RA, Kulagin IA, Ryasnyansky AI, Tugushev RI, Usmanov T (2004) Characterization of nonlinear optical parameters of KDP, LiNbO3 and BBO crystals. *Opt Commun* 229(1–6):403–412.
20. del Coso R, Requejo-Isidro J, Solis J, Gonzalo J, Afonso CN (2004) Third order nonlinear optical susceptibility of Cu:Al_2O_3 nanocomposites: From spherical nanoparticles to the percolation threshold. *J Appl Phys* 95(5):2755–2762.
21. Xenogiannopoulou E, et al. (2008) Third-order nonlinear optical response of gold-island films. *Adv Funct Mater* 18(8):1281–1289.
22. Garcia HA, Correia GB, de Oliveira RJ, Galembeck A, de Araújo CB (2012) Third- and fifth-order susceptibilities of cobalt oxide nanoparticles dispersed in n-heptane. *J Opt Soc Am B* 29(7):1613–1617.
23. Monteiro-Filho JB, Gómez-Malagón LA (2012) Resonant third order nonlinear optical susceptibility of gold nanoparticles. *J Opt Soc Am B* 29(7):1793–1798.
24. Renger J, Quidant R, van Hulst N, Novotny L (2010) Surface-enhanced nonlinear four-wave mixing. *Phys Rev Lett* 104(4):046803.
25. Palomba S, Novotny L (2008) Nonlinear excitation of surface plasmon polaritons by four-wave mixing. *Phys Rev Lett* 101(5):056802.
26. Renger J, Quidant R, van Hulst N, Palomba S, Novotny L (2009) Free-space excitation of propagating surface plasmon polaritons by nonlinear four-wave mixing. *Phys Rev Lett* 103(26):266802.
27. Danckwerts M, Novotny L (2007) Optical frequency mixing at coupled gold nanoparticles. *Phys Rev Lett* 98(2):026104.
28. Johnson PB, Christy RW (1972) Optical constants of the noble metals. *Phys Rev B* 6(12): 4370–4379.